Applied Clay Science 186 (2020) 105450

Contents lists available at ScienceDirect

Applied Clay Science

journal homepage: www.elsevier.com/locate/clay

Research Paper

A novel halloysite–CeO_x nanohybrid for efficient arsenic removal

Yaran Song[a,b], Peng Yuan[a,*], Peixin Du[a], Liangliang Deng[a], Yanfu Wei[c], Dong Liu[a], Xuemin Zhong[a,b], Junming Zhou[a,b]

[a] CAS Key Laboratory of Mineralogy and Metallogeny/Guangdong Provincial Key Laboratory of Mineral Physics and Materials, Guangzhou Institute of Geochemistry, Institutions of Earth Science, Chinese Academy of Sciences (CAS), Guangzhou 510640, China
[b] University of Chinese Academy of Sciences, Beijing 100049, China
[c] Key Laboratory of Theoretical Chemistry of Environment, Ministry of Education; School of Chemistry and Environment, South China Normal University, Guangzhou 510006, China

ARTICLE INFO

Keywords:
Halloysite
CeO_2 nanoparticles
NaOH etching
As(III)
Adsorption

ABSTRACT

In this work, halloysite-CeO_x (x = 1.5–2.0) nanocomposites were prepared using a redox-precipitation method, and the As(III) removal performance of the obtained materials was evaluated. These composites were formed by supporting CeO_2 nanoparticles on the chemically modified halloysite substrate. The modification of halloysite using a facile NaOH treatment dramatically increased the inner-surface and inner hydroxyl groups. These increased groups significantly enhanced the dispersion of the coating of CeO_2 nanoparticles due to electrostatic interactions. The specific surface area and pore volume of the optimized $Hal_{0.01}Ce$ composite was 91.1 m^2/g and 0.16 cm^3/g, respectively. This composite exhibited an excellent As(III) adsorption capacity (209.3 mg/g CeO_2), which was much higher than the unmodified halloysite-CeO_x composite (158.5 mg/g CeO_2) and unsupported CeO_2 nanoparticles (61.9 mg/g). The As(III) adsorption mechanisms on this composite involved the formation of surface complexes and oxidation of partial As(III) followed by As(V) adsorption. In addition, the $Hal_{0.01}Ce$ composite also possessed selective adsorption for As(III) in the presence of coexisting ions and maintained 91.4% of the As(III) removal efficiency after three regeneration cycles. These results demonstrate that this composite can be used as a potential candidate for As(III) removal from contaminated water.

1. Introduction

Arsenic is recognized as one of the most toxic elements in aquatic environments (Liu et al., 2019). In particular, excessive arsenic in drinking water has become a worldwide problem, which can cause serious damage to human skin, liver, kidneys, and lungs (Jang et al., 2006; Wang and Mulligan, 2006). In view of its adverse effects, an upper limit of 10 μg/L in drinking water has been mandated according to the guidelines of the World Health Organization (WHO) (Zhang et al., 2003; Shehzad et al., 2019). In natural water, arsenic primarily presented in its inorganic states, which have two significant species: arsenite (As(III)) and arsenate (As(V)) (Shehzad et al., 2019). Compared with As(V), As(III) is more toxic, mobile, and difficult to remove due to its uncharged species (H_3AsO_3) at the pH values of natural water (Chen et al., 2018). Previous studies have reported that As(III) is up to 60 times more toxic than As(V) (Maity et al., 2005; Song et al., 2019). Therefore, there is an urgent demand to develop efficient methods to remove As(III) from aqueous solutions.

Among the numerous As(III) removal technologies, adsorption has been considered as an attractive alternative due to its high efficiency, operational simplicity, and cost-effectiveness (Wei et al., 2009; Fu et al., 2018a; Fu et al., 2018b). Various adsorbents have been used for As(III) removal, such as metal oxides (Kunzru and Chaudhuri, 2005; Zhang et al., 2017a; Shehzad et al., 2019), natural minerals (Jang et al., 2006; Jang et al., 2007), carbon nanotubes (Peng et al., 2005), and ion exchange resins (He et al., 2012), among others. In particular, cerium-based hybrid materials have attracted increasing attention as a potential and efficient adsorbent for As(III) because of its advantages of high affinity and effective selectivity (Liu et al., 2018; Banerjee and Sharma, 2019). Cerium oxides or cerium-based materials have a strong interaction with As(III) by surface complexation and oxidation-reduction reactions (Chen et al., 2018; Zhang et al., 2016). For example, cerium-loaded chitosan-polyvinyl alcohol composite nanofiber (Sharma et al., 2014), anion-exchanger-supported nanoceria (Shan et al., 2019), and cerium-incorporated manganese oxide (Gupta et al., 2012) have been prepared for As(III) removal. However, these hybrid adsorbents still

* Corresponding author at: CAS Key Laboratory of Mineralogy and Metallogeny, Guangzhou Institute of Geochemistry, Chinese Academy of Sciences (CAS), Wushan, Guangzhou 510640, China.
E-mail address: yuanpeng@gig.ac.cn (P. Yuan).

https://doi.org/10.1016/j.clay.2020.105450
Received 18 November 2019; Received in revised form 10 January 2020; Accepted 12 January 2020

face the problems of an inhomogeneous distribution of the supporting nanoparticles, and they possessed a low adsorption capacity and a weak binding affinity for As(III). To increase the dispersibility of nanoparticles that are accessible for As(III) capture, a hybrid material combining cerium oxide with porous support is highly desirable for effective As(III) removal.

Halloysite, a natural 1:1 aluminosilicate mineral, has a similar chemical composition as kaolinite. The unit layer of halloysite is formed by the stacking of oxygen-sharing tetrahedral SiO_4 sheets and octahedral AlO_6 sheets (Deng et al., 2017). The monolayer water molecules are filled in the interlayer of halloysite to form hydrated halloysite (Halloysite-10 Å), which could transform to dehydrated halloysite (Halloysite-7 Å) by the deprivation of interlayer water (Tan et al., 2014). Generally, halloysite has a unique nanotubular morphology with a length of 0.02–30 μm, an internal diameter ranging from 10 to 100 nm, and an outer diameter ranging from 30 to 90 nm (Tan et al., 2013). The tubular structure possesses different groups in the external surface (Si − O − Si) and the inner surface (Al − OH), resulting in different activities on its inner and outer surfaces (Du et al., 2018). For example, halloysite was used as a drug carrier for the loading of ibuprofen in the lumen by using hydrogen-bonded with hydroxyl groups (Tan et al., 2013). Halloysite was modified by grafting organic bilayer to prepare solvent-free nanofluids, and heat treatments were used to adjust the macroscopic liquid-like behavior near room temperature (Du et al., 2018). Because of these specific features (mesoporous lumen and the modifiable surface groups), halloysite has been demonstrated as a preferable host for supporting nanoparticles in pollutant removal (Almasri et al., 2019; Ngulube et al., 2019; Torres-Luna et al., 2019). In fact, CeO_2-based halloysite composites have been widely investigated for the catalytic degradation of pollutants (Li et al., 2015; Ye et al., 2016; Ouyang et al., 2017). However, the design of halloysite-supported cerium oxide nanoparticles as an adsorbent for As(III) has attracted little attention.

In this work, CeO_x-coated halloysite composites were prepared for As(III) removal in aqueous solution. Pretreatment of halloysite using a simple NaOH etching method was conducted to enhance the dispersibility of CeO_2 nanoparticles on halloysite. The changes in the hydroxyl groups of the halloysite under NaOH treatment were then discussed. The morphology, structure, and porosity of the composites, and the optimized dispersibility of the CeO_2 nanoparticles on the modified halloysite were also estimated using X-ray diffraction (XRD), transmission electron microscopy (TEM), and N_2 adsorption-desorption characterizations. Batch As(III) adsorption tests were then systematically performed on this composite. In addition, the As(III) adsorption mechanisms were elucidated using X-ray photoelectron spectroscopy (XPS) measurements.

2. Materials and methods

2.1. Chemicals and materials

Halloysite (Hal) sourced from Linfen, in the Shanxi Province was used after purification. NaOH, $Ce(NO_3)_3{\cdot}6H_2O$, and hexamethylenetetramine were used to prepare the composites. The As(III) solution was prepared using $NaAsO_2$. All reagents were analytical grade without any other treatment.

2.2. NaOH etching of halloysite

In a typical procedure, 1 g of Hal was mixed with 50 mL of NaOH solution of different concentrations, which were 0.01, 0.1, and 0.5 mol/L, in a plastic beaker under magnetic stirring for 24 h at room temperature. Then, the solid was collected by centrifugation and washed several times with distilled water until it reached a neutral pH. It was then freeze-dried overnight. The NaOH-etched Hal was denoted as Hal_x, where x represented the concentration of the NaOH solution.

2.3. Synthesis of the modified halloysite-CeO_x composites

The modified halloysite-CeO_x composite was prepared using a redox-precipitation method, and the synthesis steps were as follows. An amount consisting of 0.6 g of Hal_x was added to 200 mL of distilled water with ultrasonication for 30 min to make the halloysite nanotubes disperse completely. Then, 0.6 g of $Ce(NO_3)_3{\cdot}6H_2O$ was dissolved into the suspension accompanied by magnetic stirring for 30 min. Finally, 5 g of $C_6H_{12}N_4$, which was used to regulate the pH value and promote the formation of CeO_2 nanoparticles (Guo et al., 2015; Kim et al., 2014), was added into the mixture in a water bath at 90 °C for 1 h. After continuously stirring for 12 h, the precipitates were collected using centrifugation and washed several times with distilled water. The obtained precipitates were freeze-dried overnight and were denoted as Hal_xCe (x = 0.01, 0.1, and 0.5). The unmodified halloysite-CeO_x composite was synthesized using the same procedures and was denoted as HalCe.

2.4. Characterization methods

The diffuse reflectance infrared Fourier-transform (DRIFT) spectra were collected using a Bruker VERTEX70 Fourier transforms infrared spectroscopy. All obtained spectra were corrected by KBr background and collected in the range of 600–4000 cm^{-1} with a resolution of 2 cm^{-1}. The XRD patterns were measured on a Bruker D8 Advance diffractometer with a Ni filter and Cu Kα radiation (λ = 0.154 nm) operating at 40 KV and 40 mA. The scan rate of the instrument was 3° (2θ)/min. The N_2 adsorption-desorption tests were conducted on a Micromeritics ASAP 2020 system. The samples were outgassed at 250 °C for 12 h before the measurement. The specific surface area (S_{BET}) was evaluated using the multiple-point Brunauer–Emmett–Teller (BET) method, and the total pore volume (V_{pore}) was calculated according to the N_2 adsorption at a relative pressure of approximately 0.99. The pore size distribution (PSD) was computed using the Barrett-Joyner-Halenda (BJH) method. The TEM images were acquired on an FEI Talos F200 s electron microscope at 200 kV. The XPS analysis was operated using a Thermo Fisher K-Alpha instrument equipped with an Al Kα source. The pass energy of wide scanning and narrow scanning was set to 100 eV and 30 eV, respectively. The binding energies of all peaks were corrected according to the C1s with a position at 284.8 eV.

2.5. As(III) adsorption measurements

The As(III) adsorption tests were conducted in 50 mL centrifugal tubes that included 50 mg of adsorbents and 20 mL of As(III) solution at room temperature (25 °C). The centrifugal tubes were shaken in an oscillator at 200 rpm for 24 h. The As(III) concentration in the solution was calculated using an inductively coupled plasma optical emission spectrometer (ICP-OES, VARIAN VISTA PRO). Blank and parallel tests were also conducted. The amount of As(III) adsorbed per unit mass of the adsorbent, q (mg/g), was computed using Eq. (1):

$$q = \frac{(C_0 - C_t) \times V}{m} \quad (1)$$

where C_0 (mg/L) is the initial concentration of As(III); C_t (mg/L) is the residual concentration of As(III) at any time; V (mL) is the volume of the solution; and m (mg) is the quality of the adsorbent.

In the adsorption isotherm experiment, the As(III) concentration ranged from 10 to 300 mg/L. For the pH effect test, the pH value of the As(III) solution was regulated from 2.0 to 12.0 using 0.1 mol/L NaOH and HCl solution. In the kinetics test, the As(III) concentration was measured at various times at a pH value of 7.0. 50 and 100 mg/L of competition ions (Na^+, K^+, Cl^-, NO_3^-, HCO_3^-, and SO_4^{2-}) were chosen to estimate the selective adsorption for As(III) on the adsorbent. The regeneration capacity of the adsorbent was conducted for three cycles using 1 mol/L NaOH desorption solution.

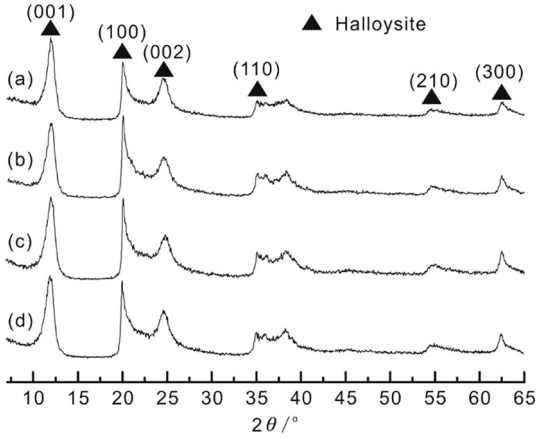

Fig. 1. XRD patterns of (a) Hal, (b) $Hal_{0.01}$, (c) $Hal_{0.1}$, and (d) $Hal_{0.5}$.

3. Results and discussion

3.1. Structural changes in the NaOH etching of the halloysite

The XRD patterns of Hal, $Hal_{0.01}$, $Hal_{0.1}$, and $Hal_{0.5}$ are shown in Fig. 1. Hal showed the *d*-values of 0.740, 0.444, and 0.363 nm (Fig. 1a), which corresponded to the (001), (100), and (002) reflections of halloysite. The d_{001}-value of Hal was 0.740 nm, indicating that Hal was identified as Halloysite-7 Å. As shown in Fig. 1b – d, the Hal reflections were observed in the XRD patterns of Hal_x, indicating that the crystalline structure of the halloysite was well preserved after NaOH treatment. Compared with the (100) reflections, the intensity of the (001) reflections in Hal_x reduced after NaOH etching. This result indicated that the NaOH etching of Hal induced a disorder of the *c* axis; however, the *a* planes order was preserved.

DRIFT is a powerful tool for the detection of the hydroxyl groups stretching vibrations of silicate minerals (Yuan et al., 2012b). The changes in the hydroxyl groups of NaOH-modified halloysite were studied using DRIFT (Fig. 2). In the DRIFT spectrum of Hal (Fig. 2a), the 3699 and 3627 cm^{-1} bands were assigned to the stretching vibration of the inner-surface hydroxyl groups and inner hydroxyl groups, respectively (Yuan et al., 2012b). The DRIFT spectrum of $Hal_{0.01}$ (Fig. 2b) displayed no evident change, which might be due to the small variations of Hal after mild NaOH etching, which were hardly detected. However, the previous study reported that increased hydroxyl groups on the halloysite were observed after a low concentration of NaOH treatment (0.015 mol/L) (Zeng et al., 2014). The intensity of the 3699 and 3627 cm^{-1} bands was substantially increased in the spectra of $Hal_{0.1}$ (Fig. 2c) and $Hal_{0.5}$ (Fig. 2d), indicating that the inner-surface and inner hydroxyl groups were significantly increased with an increase in the NaOH concentration. The adsorption band at 903 and 997 cm^{-1} observed in the spectrum of Hal was attributed to the weakly hydrogen-bonded inner-surface hydroxyl groups and Si – O stretching vibration (Frost et al., 1999; Johansson et al., 1999). However, the 903 cm^{-1} band was difficult to observe in the spectrum of $Hal_{0.5}$, indicating that a partial amount of the inner-surface hydroxyl groups were removed during the drastic NaOH etching. The 997 cm^{-1} band for Hal was toward higher wavenumbers (1006 cm^{-1}) in the $Hal_{0.5}$ spectrum, which was probably assigned to the silicon-rich nanoparticles (White et al., 2012). This result suggested that the Si – O bonds of Hal were attacked by the NaOH treatment.

Table 1
Contents of the dissolved Si and Al in the solution.

Samples	Dissolved Si (mg/L)	Dissolved Al (mg/L)
$Hal_{0.01}$	12.96	6.98
$Hal_{0.1}$	85.58	78.50
$Hal_{0.5}$	335.50	252.70

Previous studies had reported that a high concentration of NaOH treatment (> 1 mol/L) after a long duration or heating treatment might damage the structural integrity and mechanical performance of halloysite, limiting its further practical application (Zeng et al., 2014). Therefore, the surface modification of halloysite was conducted using a low NaOH concentration (≤ 0.5 mol/L) at room temperature. As shown in Table 1, the amount of dissolved Al and Si significantly increased with an increase in the NaOH concentration. Combined with the above-mentioned results, the Al—OH and Si—O bonds were attacked by the NaOH treatment, resulting in the generation of broken Al—O and Si—O bonds on halloysite. The hydroxyl groups were formed by the protonation of these broken bonds.

3.2. Effects of NaOH etching on the preparation of halloysite-CeO_x composites

The XRD patterns of CeO_2, $Hal_{0.01}Ce$, $Hal_{0.1}Ce$, and $Hal_{0.5}Ce$ are shown in Fig. 3. The XRD pattern of CeO_2 (Fig. 3a) exhibited *d*-values of 0.311, 0.269, 0.191, 0.163, and 0.135 nm, which were in agreement with the (111), (200), (220), (311), and (400) reflections of the fluorite structure (JCPDS No. 34-0394), respectively. The HalCe (Fig. 3b) and Hal_xCe (Fig. 3c – e) composites exhibited a decreased intensity in the reflections of halloysite, which might be due to the incorporation of CeO_2 in the halloysite substrate. In particular, the intensity of the (001) reflections in the Hal_xCe composites was substantially weakened. This result indicated the adverse effects of the *c* axis order due to the coating of the CeO_2 nanoparticles on the halloysite.

The TEM image of Hal (Fig. 4a) showed that the halloysite particles had typical cylindrical shapes and the cylinders were hollow and open-

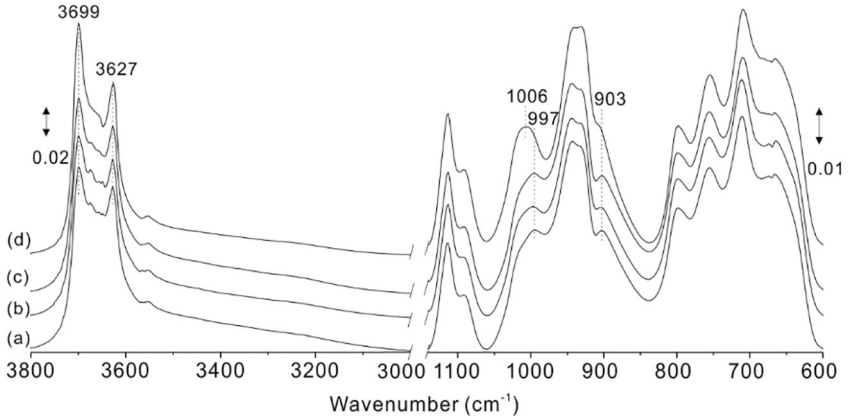

Fig. 2. DRIFT spectra of (a) Hal, (b) $Hal_{0.01}$, (c) $Hal_{0.1}$, and (d) $Hal_{0.5}$.

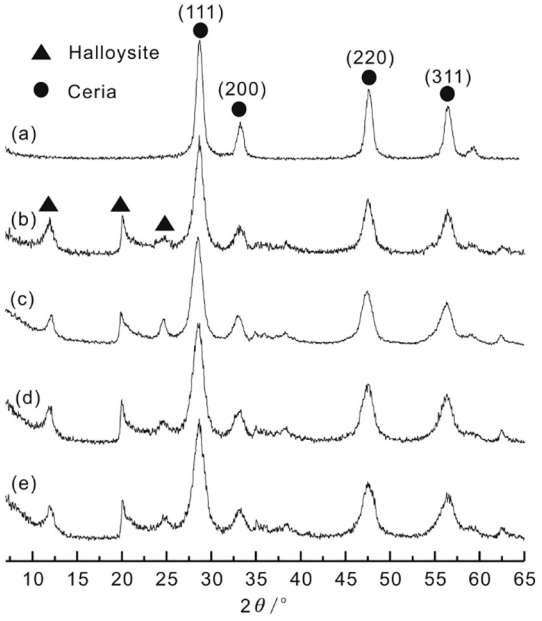

Fig. 3. XRD patterns of (a) CeO_2, (b) HalCe, (c) $Hal_{0.01}Ce$, (d) $Hal_{0.1}Ce$, and (e) $Hal_{0.5}Ce$.

ended. The lengths of the halloysite nanotubes ranged from approximately about 0.2–1 μm and the inner diameters were about 20–50 nm. As shown in the TEM image of CeO_2 (Fig. 4b), the CeO_2 nanoparticles possessed quadrilateral-like morphologies. The nanoparticles had particle sizes that ranged from 5 to 10 nm and evidently aggregated together. From the TEM image of HalCe (Fig. 4c), the CeO_2 nanoparticles were loaded on the surface and inner nanotube of the halloysite. However, the coating particles were unevenly dispersed and partially agglomerated. The TEM image of $Hal_{0.01}Ce$ (Fig. 3d) displayed that the tubular morphology of the halloysite remained largely intact after NaOH treatment. The CeO_2 nanoparticles exhibited an incremental load amount and uniform distribution on the particles of the halloysite. This phenomenon might be due to an increase in the hydroxyl groups in the NaOH etching of the halloysite. The high-resolution TEM (HRTEM) image of $Hal_{0.01}Ce$ (Fig. 4e) exhibited that the interplanar distance of the nanoparticle was 0.314 nm corresponding to the (111) reflection of the CeO_2 according to JCPDS reference data (NO. 34-0394). With an increase in the NaOH etching concentration, the nanotubular structures were also well preserved in the $Hal_{0.1}Ce$ (Fig. 4f) and $Hal_{0.5}Ce$ (Fig. 4g) composites. More load amounts and coacervates of the CeO_2 nanoparticles were observed in the $Hal_{0.1}Ce$ and $Hal_{0.5}Ce$ composites than those in the $Hal_{0.01}Ce$ composite.

The nitrogen adsorption–desorption isotherms and pore size distribution (PSD) curves of the materials are presented in Fig. 5 and the S_{BET} and V_{pore} values of the materials are shown in Table 2. The isotherm of Hal was classified as type IV with an H3 hysteresis loop according to the International Union of Pure and Applied Chemistry (IUPAC) classification (Thommes et al., 2015). Hal exhibited an evident hysteresis loop, indicating that halloysite had massive mesoporous structures. The PSD curve of Hal showed two primary pore distributions centered at 15.0 and 42.0 nm. These 15.0 nm mesopores might be derived from the lumens of the halloysite. The 42.0 nm mesopores might have originated from the interparticle porosity between the halloysite nanotubes (Yuan et al., 2012b). These results were in agreement with the previous TEM results (Fig. 4a). The isotherm of CeO_2 belonged to type II with an H3 hysteresis loop. A large hysteresis loop of the CeO_2 indicated the presence of numerous mesopores, which were identified as the stacked spaces between the CeO_2 nanoparticles. The peak at 7 nm in the PSD curve of CeO_2 represented the primary population of these mesopores. The Hal_xCe composites exhibited an isotherm of type IV with an H3 hysteresis loop, indicating that these composites primarily had mesoporous structures with a small amount of micropores. Compared with CeO_2, minor hysteresis loops and no dramatic peaks were observed in the isotherms and PSD curves of the composites. These results indicated that the interspaces between the CeO_2 nanoparticles were significantly reduced resulting from the homogeneous dispersion of CeO_2 nanoparticles on the halloysite substrate. The mesoporous distribution and hysteresis loops of the Hal_xCe composites were significantly weakened but remained resolvable, indicating that CeO_2 nanoparticles were loaded on the external surface and in the lumens of halloysite, however, these lumens of the nanotubes were not completely blocked.

The S_{BET} value of $Hal_{0.01}Ce$ (91.1 m^2/g) was higher than that of Hal (56.5 m^2/g), CeO_2 (86.4 m^2/g), and HalCe (85.8 m^2/g), which might be due to the uniform distribution of CeO_2 nanoparticles on the halloysite and the presence of a small amount of micropores. Compared with $Hal_{0.01}Ce$, $Hal_{0.1}Ce$ and $Hal_{0.5}Ce$ exhibited lower S_{BET} values of 83.9 and 81.7 m^2/g, respectively. Combined with the TEM results (Fig. 4d − g), this decrease might be due to the obvious agglomeration of the coating CeO_2 nanoparticles, resulting in the blockage of the lumens of the halloysite nanotubes and a reduction of the porosity of the composites. The V_{pore} values of $Hal_{0.01}Ce$, $Hal_{0.1}Ce$, and $Hal_{0.5}Ce$ were 0.16, 0.15, and 0.15 cm^3/g, respectively, which were smaller than that of Hal. The decreased porosity might be due to the load of CeO_2 nanoparticles on the halloysite, filling its lumens and the spaces between the halloysite particles.

The above-mentioned results indicated that the NaOH modification of halloysite was favorable for increasing the load and dispersibility of CeO_2 nanoparticles on the surface and in the lumen of halloysite. This might be attributed to the increased hydroxyl groups on the modified halloysite. For Hal_x, the hydroxyl groups had two forms of ionization reaction in aqueous solution (Yuan et al., 2012a):

$$Si/AlOH + H^+ \rightarrow Si/AlOH_2^+$$

$$Si/AlOH \rightarrow Si/AlO^-$$

The surface charges of hydroxyl groups depended on the pH value of the solution. In addition, Ce^{3+} can remain stable in a weakly acidic environment. However, the redox reaction of Ce^{3+} occurred with an increase in pH value (Guo et al., 2015). Under the loading conditions (pH ~ 9.0), the deprotonated hydroxyl groups of the halloysite were negatively charged (Yuan et al., 2012a), which had a high affinity with positively charged Ce^{3+}/Ce^{4+} due to electrostatic attraction. Then, the redox precipitation of the anchored Ce^{3+}/Ce^{4+} occurred, followed by the hydrolysis of hexamethylenetetramine, resulting in the coating of the CeO_2 nanoparticles on the halloysite. Because of the increased hydroxyl groups, the modified halloysite had more interaction sites to react with CeO_2 nanoparticles than the unmodified halloysite, leading to an enhancement of load and distribution of CeO_2 nanoparticles on the halloysite.

3.3. As(III) adsorption performance

3.3.1. Adsorption isotherms

The As(III) adsorption isotherms and the fitting parameters of Hal, Hal_x, CeO_2, Hal_xCe, and HalCe are displayed in Fig. 6 and Table 3, respectively. The Langmuir isotherm model (Eq. (2)), Freundlich isotherm model (Eq. (3)), and Dubinin-Radushkevich (D-R) isotherm model (Eqs. (4–5)) are applied to describe the isotherm adsorption results (Zhang et al., 2017b; Ijagbemi et al., 2010; Bian et al., 2018):

$$q_e = \frac{Q_m K_L C_e}{1 + a_L C_e} \quad (2)$$

$$\ln(q_e) = \ln(k_f) + \left(\frac{1}{n}\right)\ln(C_e) \quad (3)$$

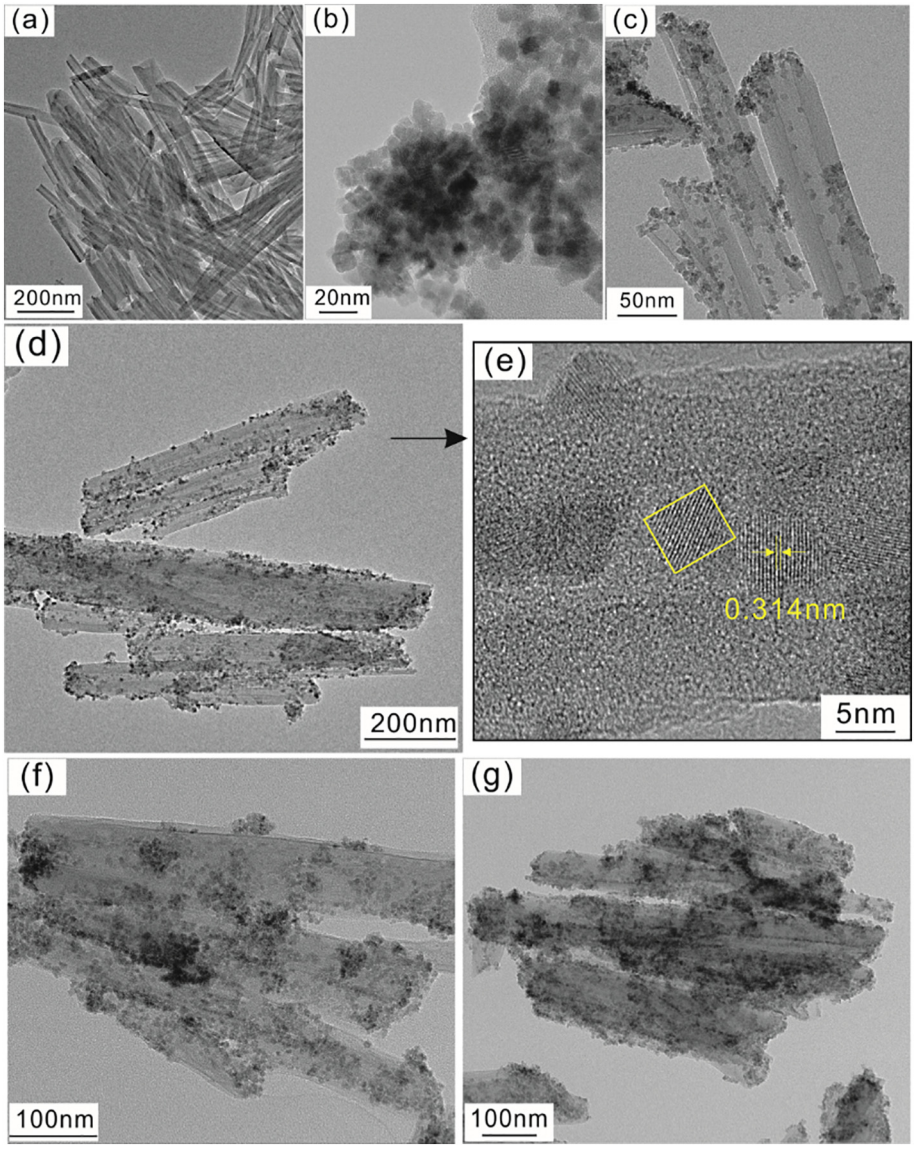

Fig. 4. The TEM images of (a) Hal, (b) CeO_2, (c) HalCe, (d) $Hal_{0.01}Ce$, (e) the HRTEM image of $Hal_{0.01}Ce$, the TEM images of (f) $Hal_{0.1}Ce$, and (g) $Hal_{0.5}Ce$.

$$\ln(q_e) = \ln(q_m) - k\varepsilon^2 \quad (4)$$

$$\varepsilon = \mathrm{RTln}\left(1 + \frac{1}{C_e}\right) \quad (5)$$

$$\mathrm{E} = \frac{1}{\sqrt{2k}} \quad (6)$$

where q_e (mg/g) represents the adsorption capacity of the adsorbents at equilibrium; Q_m represents the As(III) monolayer adsorption capacity;

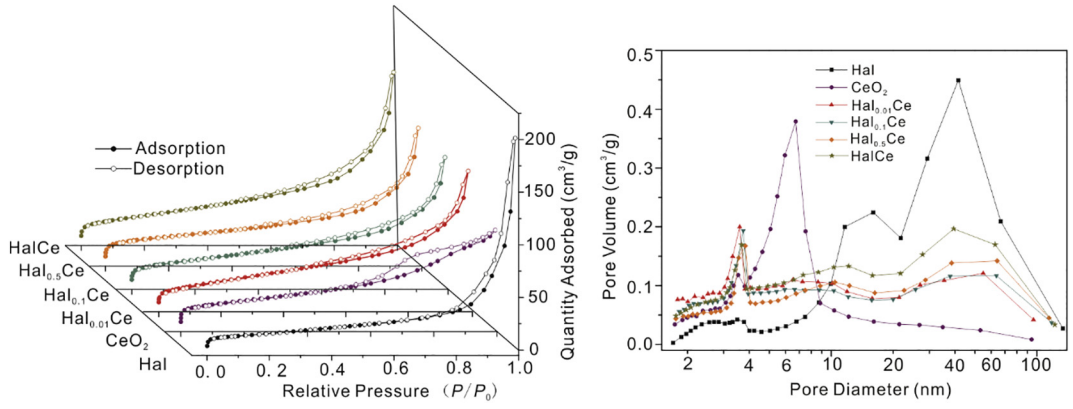

Fig. 5. Nitrogen adsorption–desorption isotherms and PSD curves of Hal, CeO_2, HalCe, and Hal_xCe.

Table 2
The S_{BET} and V_{pore} values of Hal, CeO_2, HalCe, and Hal_xCe.

Samples	S_{BET} (m^2/g)	V_{pore} (cm^3/g)
Hal	56.5	0.20
CeO_2	86.4	0.13
$Hal_{0.01}Ce$	91.1	0.16
$Hal_{0.1}Ce$	83.9	0.15
$Hal_{0.5}Ce$	81.7	0.15
HalCe	85.8	0.18

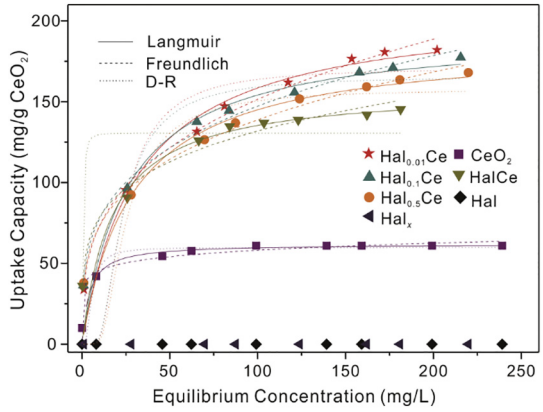

Fig. 6. The As(III) adsorption isotherms of Hal, Hal_x, CeO_2, HalCe, and Hal_xCe.

Table 3
The Langmuir, Freundlich, and D-R fitting results and CeO_2 content of CeO_2, HalCe, and Hal_xCe.

		$Hal_{0.01}Ce$	$Hal_{0.1}Ce$	$Hal_{0.1}Ce$	HalCe	CeO_2
Langmuir	$Q_{m\text{-}s}$ (mg/g)	209.3	193.8	187.0	158.5	61.9
	K_L (L/mg)	0.031	0.038	0.035	0.058	0.248
	R^2	0.946	0.929	0.909	0.902	0.963
Freundlich	K_f (L/g)	35.1	41.0	38.4	46.7	35.9
	n	3.15	3.60	3.58	4.44	9.58
	R^2	0.993	0.992	0.993	0.974	0.964
D-R	K (mol^2/kJ^2)	0.0099	0.0095	0.0112	–	0.0006
	Q_m (mg/g)	170.9	165.6	157.9	130.6	59.7
	E (kJ/mol)	7.11	7.25	6.68	–	28.87
	R^2	0.855	0.857	0.823	0.755	0.934
CeO_2[a] (%wt)		26.35	25.10	23.89	26.63	–

[a] Was calculated by ICP-OES.

C_e (mg/L) is the As(III) equilibrium concentration; and K_L and a_L are the adsorption equilibrium constants. $Q_{m\text{-}s}$ represents the As(III) adsorption capacity normalized by the CeO_2 content. K_f (L/mg) and n are Freundlich constants. k (mol^2/kJ^2) is the D–R constant; R is the molar gas constant (8.314 J/K mol); T is the temperature of solution; E (kJ/mol) represents the mean free energy of adsorption, which was calculated by the Eq. (6).

As shown in Table 3, the isotherm adsorption data of all adsorbents were fitted well with the Langmuir and Freundlich isotherm models (correlation coefficient $R^2 > 0.900$). The R^2 values of the Freundlich model were higher than those of the Langmuir and D–R models, indicating that the adsorbents had heterogeneous surfaces with adsorption sites that had different adsorption energies. The maximum adsorption capacities of all adsorbents achieved by the Langmuir model were higher than those fitted by the D–R model, indicating that the As (III) adsorption on the surface of the adsorbents possessed various adsorption mechanisms. The monolayer adsorption capacity $Q_{m\text{-}s}$ of the adsorbents followed an order of $Hal_{0.01}Ce$ (209.3 mg/g CeO_2) > $Hal_{0.1}Ce$ (193.8 mg/g CeO_2) > $Hal_{0.5}Ce$ (187.0 mg/g CeO_2) > HalCe (158.5 mg/g CeO_2) > CeO_2 (61.9 mg/g). The As(III) adsorption capacity of pristine Hal and Hal_x was too extremely low to be overlooked. The adsorption capacity of $Hal_{0.01}Ce$ was three times higher than that of CeO_2, indicating that the supporting of the halloysite host significantly increased the adsorption capacity of the CeO_2 nanoparticles. Compared with other composites, $Hal_{0.01}Ce$ exhibited a superior As(III) adsorption capacity, suggesting that the uniformly distributed CeO_2 nanoparticles on the halloysite substrate provided abundant active adsorption sites and generated a small amount of micropores, resulting in the efficient As(III) removal. In addition, the As (III) adsorption capacity of $Hal_{0.01}Ce$ was higher than those of the previously reported adsorbents (Table 4).

3.3.2. Adsorption mechanisms

Due to the uniform dispersion of CeO_2 nanoparticles and high As (III) adsorption performance, the $Hal_{0.01}Ce$ composite was chosen to investigate the As(III) adsorption mechanisms in this study. XPS measurements were performed to illustrate the changes in the surface chemical states of this composite before and after As(III) adsorption (Fig. 7). The O1s XPS spectra of $Hal_{0.01}Ce$ composite before and after As (III) adsorption are presented in Fig. S1. As shown in Fig. S1a, the O1s spectrum was divided into three peaks at 528.91, 531.61, and 532.82 eV, which were assigned to the lattice oxygen (M–O), hydroxyl group (Ce–OH), and surface adsorbed water (H_2O), respectively (Yu et al., 2017; Chen et al., 2018). After As(III) adsorption, the proportion of the peak at binging energy of 532.40 eV significantly increased (Fig. S1b), indicating As had been adsorbed on the surface of the composite (Zhang et al., 2010). The reduction of Ce–OH was observed in the As (III) adsorbed $Hal_{0.01}Ce$ ($Hal_{0.01}Ce$–As), suggesting that the Ce–OH can be replaced by arsenite species.

The Ce3d XPS spectra before and after As(III) adsorption are presented in Fig. 7a − b. The Ce3d region had separated spin-orbit split doublets that represented the $Ce3d_{5/2}$ (denoted as V) and $Ce3d_{3/2}$ (denoted as U) components, respectively. As shown in Fig. 7a, the fitted peaks of Ce3d in $Hal_{0.01}Ce$ centered at 882.50, 901.09, 888.86, 907.76, 898.09, and 916.39 eV, which were referred to as V, U, V_2, U_2, V_3, and U_3, respectively, were attributed to quadrivalent Ce(IV) (Beche et al., 2008). The remaining four peaks were denoted as V_0 (881.05 eV), U_0 (898.65 eV), V_1 (885.70 eV), and U_1 (904.45 eV), representing the trivalent Ce(III) (Bera and Anandan, 2014). A shift in the Ce3d spectrum was observed in the $Hal_{0.01}Ce$–As, indicating that the surface Ce − OH strongly bonded with the As(III) species to form Ce − O − As surface complexes (Fig. 7b). In addition, the proportion of Ce(III) increased from 25.29% to 35.30% after As(III) adsorption, suggesting that

Table 4
Comparison of the As(III) adsorption capacity of $Hal_{0.01}Ce$ and other reported adsorbents.

Adsorbents	Maximum adsorption capacity (mg/g)	Reference
$Hal_{0.01}Ce$	209.3	This work
Fe–Mn–Ce oxide-modified biochar	8.7	Liu et al. (2019)
Zn/Ce bimetallic oxide	88.5	Banerjee and Sharma (2019)
Cerium oxide modified activated carbon	36.8	Yu et al. (2017)
Cerium modified chitosan	57.5	Zhang et al. (2016)
Zirconia nanostructure	105.0	Shehzad et al. (2019)
CeO_2–ZrO_2 nanospheres	9.2	Xu et al. (2013)

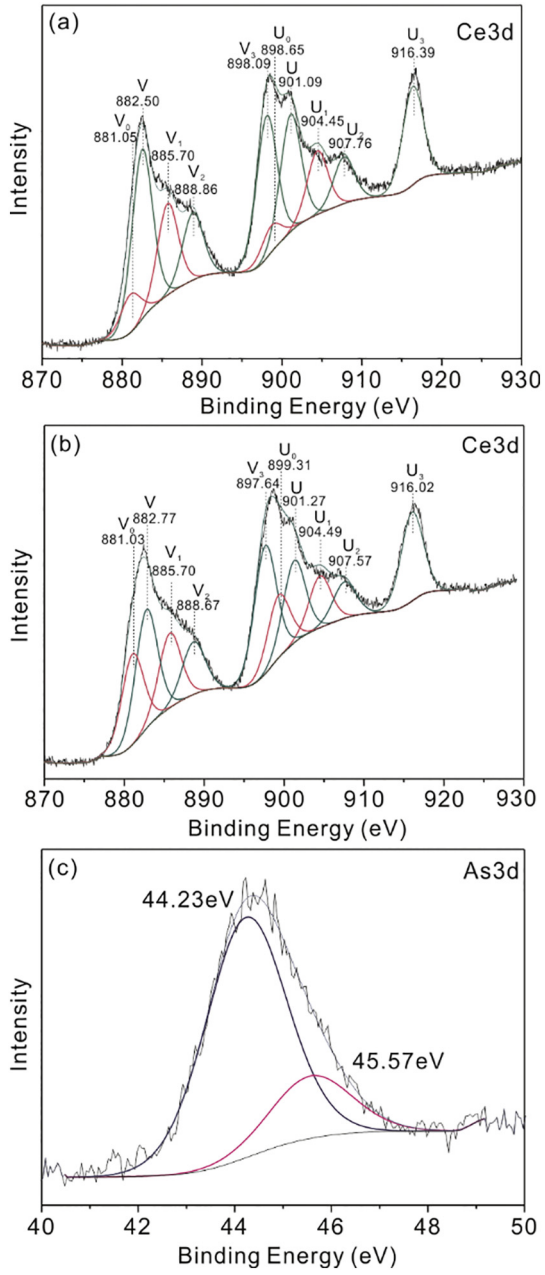

Fig. 7. The XPS spectra of $Hal_{0.01}Ce$ before and after As(III) adsorption: (a) Ce3d spectrum before As(III) adsorption, (b) Ce3d spectrum after As(III) adsorption, and (c) As3d spectrum after As(III) adsorption.

partial Ce(IV) was reduced to Ce(III) during the adsorption process.

The As3d XPS spectrum after As(III) adsorption is shown in Fig. 7c. The As3d spectrum of $Hal_{0.01}Ce$-As was fitted with two components located at 44.23 and 45.57 eV, which were attributed to As(III) and As (V), respectively (Zhang et al., 2016). The presence of As(V) in the $Hal_{0.01}Ce$–As implied that As(III) was partially oxidized to As(V) during the adsorption reaction. The above-mentioned results suggested that the redox reaction occurred by reference to the reduction of Ce(IV) and the oxidation of As(III), which was considered as one of the adsorption mechanisms of the As(III) adsorption by the $Hal_{0.01}Ce$ composite.

From the above-mentioned discussion, the As(III) adsorption mechanism by the $Hal_{0.01}Ce$ composite was concluded that (i) As(III) species had a strong bonding interaction with the cerium groups on the composite, resulting in the formation of Ce − O − As surface complexes; (ii) As(III) was partially oxidized to As(V) followed with a reduction of Ce(IV) to Ce(III). In addition, the oxidized As(V) could have been adsorbed on the composite.

3.3.3. Effect of the solution pH value

The effect of pH value on the As(III) adsorption by $Hal_{0.01}Ce$ is shown in Fig. 8a. The As(III) adsorption capacity of the composite gradually increased in the pH range from 2.0 to 7.0 and dramatically decreased when the pH rose to 12.0. These results indicated that As(III) adsorption was pH-dependent. As the pH value below 7.0, H_3AsO_3 was the major species in the solution (Sharma and Sohn, 2009). The As(III) adsorption capability gradually increased with an increase in the pH value. This might be because H_3AsO_3 preferred to form surface complexes on the $Hal_{0.01}Ce$ composite under neutral conditions (Shehzad et al., 2019). With the pH value increased (pH > 7.0), H_3AsO_3 species gradually converted to anionic forms of $H_2AsO_3^-$ following a significant decrease of As(III) adsorption performance. As confirmed by the zeta-potential analysis (Fig. S2), the composite was negatively charged at a pH above 7.0, which was unfavorable for $H_2AsO_3^-$ adsorption through electrostatic repulsion.

3.3.4. Adsorption kinetics

To assess the removal efficiency and diffusion mechanism for As (III), the adsorption kinetics of the $Hal_{0.01}Ce$ composite were investigated at different times (Fig. 8b − c). The fitting results determined from the models are listed in Table 5. The pseudo-first-order model (Eq. (7)), pseudo-second-order model (Eq. (8)), and intra-particles diffusion model (Eq. (9)) were applied to evaluate the kinetics results of the adsorbent. The equations are expressed as (Zhu et al., 2017):

$$\ln(q_e - q_t) = \ln q_e - k_1 t \tag{7}$$

$$q_t = \frac{k_2 q_e^2 t}{1 + k_2 q_e t} \tag{8}$$

$$q_t = k_i t^{1/2} + C \tag{9}$$

where q_t represents the adsorption capacity of the adsorbent at any time (t); q_e (mg/g) represents the equilibrium adsorption capacity of the adsorbent; k_1 (min^{-1}), k_2 (g/mg·min), and k_i ($mg/g{\cdot}min^{1/2}$) are the pseudo-first-order, pseudo-second-order, and intra-particles diffusion rate constants, respectively; and C (mg/g) is the intra-particle diffusion constant, which represents the thickness of the boundary layer.

As shown in Fig. 8b, the As(III) adsorption was extremely fast at the beginning, followed by a much slower rate and finally tended toward equilibrium. In the first 2 min, a rapid As(III) adsorption was observed and approximately 89% of the adsorption capacity was achieved. Then, the adsorption equilibrium was achieved in 30 min. The rapid As(III) adsorption was attributed to the fact that the uniform dispersion of CeO_2 nanoparticles was favorable for the diffusion of the As(III) species to the active sites on the composite. As shown in Table 5, the As(III) adsorption fitted well with the pseudo-second-order model and the corresponding calculated adsorption capacity q_e (23.9 mg/g) was well consistent with the experimental value (24.4 mg/g). These fitting results indicated that the As(III) rate-limiting process was chemical adsorption involving the sharing or exchange of electrons between As(III) species and the groups of the composite.

The adsorbate transferred from an aqueous phase to an adsorbent phase was a multi-step process that included external diffusion, pore diffusion, surface diffusion, and pore surface adsorption (Wang et al., 2017). The As(III) diffusion mechanism on the $Hal_{0.01}Ce$ composite was described by the intra-particle diffusion model (Fig. 8c). The observed three-segment curves indicated the multi-step diffusion during the adsorption procedures. All the linear segments did not pass through the origin, implying that the intra-particle diffusion was not only a rate-limiting step. The first linear step implied that the external mass transfer was fast and instantaneous for the boundary layer diffusion of the As(III) species to the surface of the composite. The second stage was

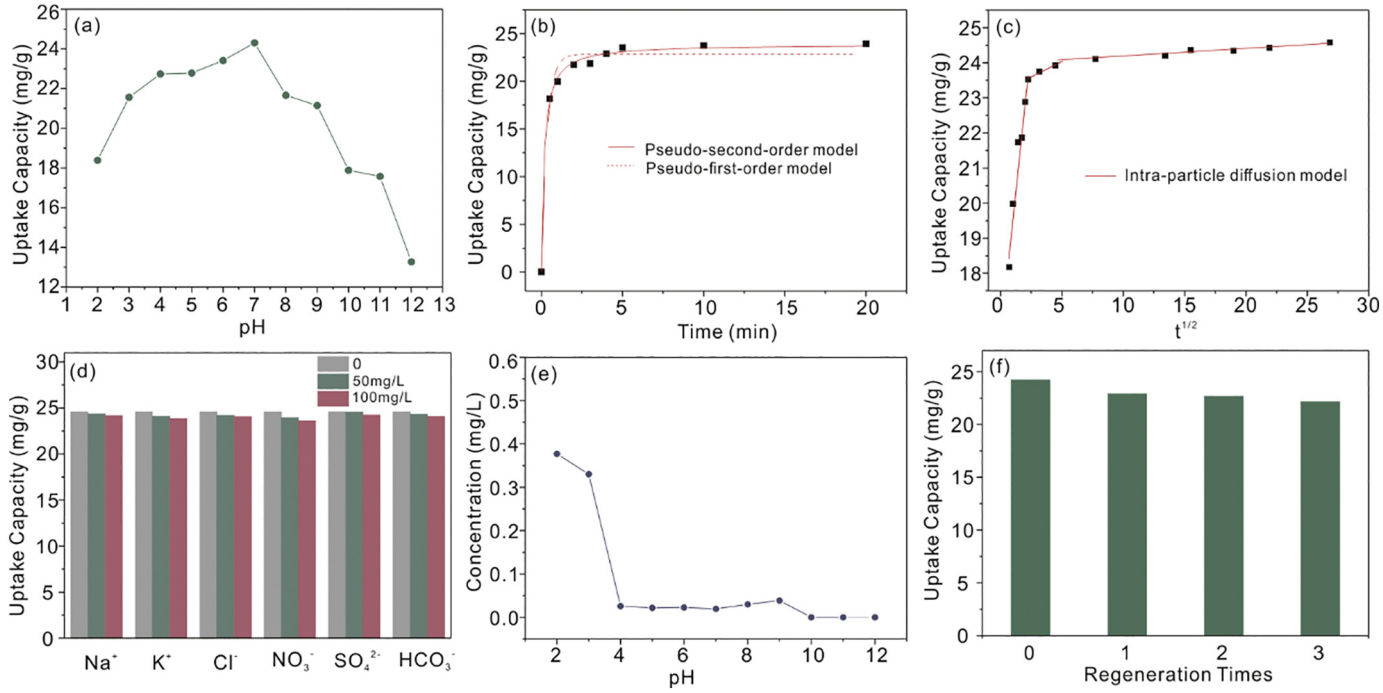

Fig. 8. The As(III) adsorption on the $Hal_{0.01}Ce$ composite: (a) the effect of initial pH values on the As(III) adsorption, (b) the pseudo-first-order and pseudo-second-order models for kinetic, (c) the intra-particle diffusion model for As(III) removal, (d) the effect of coexisting ions on As(III) removal, (e) the concentration of released cerium at pH 2.0–12.0, and (f) the regeneration results on As(III) adsorption for the three cycles.

attributed to the pore diffusion with a slow rate of 30 min, and the final step was ascribed to equilibrium adsorption.

3.3.5. *Effect of coexisting ions*

Coexisting ions, such as Na^+, K^+, Cl^-, NO_3^-, SO_4^{2-}, and HCO_3^-, might intensely occupy the active adsorption sites of the adsorbent, leading to a reduction of As(III) adsorption capability. The selective adsorption for As(III) in the presence of competing ions was performed on the $Hal_{0.01}Ce$ composite (Fig. 8d). Only a slight or negligible decrease of As(III) adsorption capacity was observed in the high concentration of competing ions, indicating that the composite exhibited insensitive adsorption selectivity for these coexistence ions. This result further provided evidence of a strong binding interaction between As (III) and the composite.

3.3.6. *Toxicity analysis*

The leaching of metal ions is a potential ecological threat of the adsorbent to natural water. The released cerium was measured at a pH range from 2.0 to 12.0 (Fig. 8e). According to the previous study, the pH value of natural water or wastewater was known to range from 6.0 to 9.0 (Xiong and Peng, 2008). The maximum concentration of released cerium by $Hal_{0.01}Ce$ composite under the pH range of natural water was 0.039 mg/L. It had been demonstrated that algae, that are at the bottom of the food chain, could be used as a sensitive indicator of toxic effects and ecological risk (Rogers et al., 2010). In the previous study, the green algae *C. reinhardtii*, which was a model of the freshwater media, had been used to evaluate the toxicity of dissolved cerium. A concentration of 50% of the maximal effect (EC_{50}) of dissolved cerium to *C. reinhardtii* was above 1.05 mg/L (Roehder et al., 2014), which was much higher than the concentration of released cerium in the $Hal_{0.01}Ce$ composite. These findings suggested that the composite used as the As (III) removal adsorbent was stable, ecological adaptability, and exhibited no harmful effects to the aquatic ecosystem.

3.3.7. *Regeneration*

The reusability of the adsorbent is believed to be one of the most significant factors for its economic use and applicability in an aqueous solution. The regeneration of the exhausted $Hal_{0.01}Ce$ composite was evaluated in the three cycles using a 1 mol/L NaOH desorption solution (Fig. 8f). At the first regeneration, 94.4% of the saturated adsorption capacity was maintained in the regenerated composite. After three subsequent cycles, the As(III) adsorption capacity slightly decreased and still remained at 91.4% of the initial value. These results indicated that the active adsorption sites of the composite were readily recovered and repeatedly reused without significant loss of the As(III) adsorption capacity.

4. Conclusions

The halloysite–CeO_x nanocomposites were synthesized by using the NaOH-modified halloysite as a substrate to support CeO_2 nanoparticles for efficient As(III) removal in an aqueous solution. Partial Si and Al were dissolved by attacking the aluminosilicate layers in the NaOH etching of the halloysite, resulting in an increase in the inner-surface and inner hydroxyl groups. These hydroxyl groups acted as “active sites” for the electrostatic attraction to uniformly anchor the CeO_2

Table 5
The pseudo-first-order, pseudo-second-order, and intra-particle diffusion fitting results of $Hal_{0.01}Ce$.

Sample	Pseudo-first-order model			Pseudo-second-order model			Intra-particle diffusion model		
	Q_e	k_1	R^2	Q_e	k_2	R^2	k_1	k_2	k_3
$Hal_{0.01}Ce$	22.8	2.868	0.981	23.9	0.242	0.997	3.317	0.175	0.025

nanoparticles on the halloysite. The $Hal_{0.01}Ce$ composite had the best dispersion of the CeO_2 nanoparticles, leading to a high specific surface area (91.1 m^2/g) and efficient As(III) adsorption capacity (209.3 mg/g CeO_2). The adsorption mechanism illustrated that As(III) was partially oxidized to As(V) coupled with As(V) adsorption, and $Ce-O-As$ surface complexes were formed. In addition, the composite also exhibited effective adsorption selectivity for As(III) against the coexisting ions, low cerium leaching in a broad pH range and excellent regeneration capability. Moreover, the halloysite-CeO_x composite also can be applied to scavenging other toxic anions from contaminated water or to the catalytic degradation of some VOC pollutants for environmental remediation.

Declaration of Competing Interests

The authors declare that they have no known competing financial interests or personal relationships that could have appeared to influence the work reported in this paper.

Acknowledgments

This work was supported by the National Natural Science Foundation of China (Grant No. 41972045 and 41672042), the National Special Support for High-Level Personnel and Youth Innovation Promotion Association CAS for the excellent members (2016-81-01) and the Science and Technology Planning Project of Guangdong Province (2017B020237003). This is a contribution No. IS-2802 from GIGCAS.

Appendix A. Supplementary data

Supplementary data to this article can be found online at https://doi.org/10.1016/j.clay.2020.105450.

References

Almasri, D.A., Saleh, N.B., Atieh, M.A., McKay, G., Ahzi, S., 2019. Adsorption of phosphate on iron oxide doped halloysite nanotubes. Sci. Rep. 9.

Banerjee, S., Sharma, Y.C., 2019. Synthesis and application of Zn/Ce bimetallic oxides for the decontamination of arsenite (As-III) ions from aqueous solutions. J. Environ. Manag. 233, 151–164.

Beche, E., Charvin, P., Perarnau, D., Abanades, S., Flamant, G., 2008. Ce3d XPS investigation of cerium oxides and mixed cerium oxide ($Ce_xTi_yO_z$). Surf. Interface Anal. 40, 264–267.

Bera, P., Anandan, C., 2014. XRD and XPS studies of room temperature spontaneous interfacial reaction of CeO_2 thin films on Si and Si_3N_4 substrates. RSC Adv. 4, 62935–62939.

Bian, L., Nie, J., Jiang, X., Song, M., Dong, F., Li, W., Shang, L., Deng, H., He, H., Xu, B., 2018. Selective removal of uranyl from aqueous solutions containing a mix of toxic metal ions using core–shell MFe_2O_4–TiO_2 nanoparticles of montmorillonite edge sites. ACS Sustain. Chem. Eng. 6, 16267–16278.

Chen, J., Wang, J., Zhang, G., Wu, Q., Wang, D., 2018. Facile fabrication of nanostructured cerium-manganese binary oxide for enhanced arsenite removal from water. Chem. Eng. J. 334, 1518–1526.

Deng, L., Yuan, P., Liu, D., Annabi-Bergaya, F., Zhou, J., Chen, F., Liu, Z., 2017. Effects of microstructure of clay minerals, montmorillonite, kaolinite and halloysite, on their benzene adsorption behaviors. Appl. Clay Sci. 143, 184–191.

Du, P., Liu, D., Yuan, P., Deng, L., Wang, S., Zhou, J., Zhong, X., 2018. Controlling the macroscopic liquid-like behaviour of halloysite-based solvent-free nanofluids via a facile core pretreatment. Appl. Clay Sci. 156, 126–133.

Frost, R.L., Kristof, J., Paroz, G.N., Kloprogge, J.T., 1999. Intercalation of kaolinite with acetamide. Phys. Chem. Miner. 26, 257–263.

Fu, H.R., Wang, N., Qin, J.H., Han, M.L., Ma, L.F., Wang, F., 2018a. Spatial confinement of a cationic MOF: a SC–SC approach for high capacity Cr(VI)-oxyanion capture in aqueous solution. Chem. Commun. 54, 11645–11648.

Fu, H.R., Zhao, Y., Zhou, Z., Yang, X.G., Ma, L.F., 2018b. Neutral ligand TIPA-based two 2D metal–organic frameworks: ultrahigh selectivity of C_2H_2/CH_4 and efficient sensing and sorption of Cr(VI). Dalton Trans. 47, 3725–3732.

Guo, S., Sun, W.Z., Yang, W.Y., Xu, Z.C., Li, Q., Shang, J.K., 2015. Synthesis of Mn_3O_4/CeO_2 hybrid nanotubes and their spontaneous formation of a paper-like, free-standing membrane for the removal of arsenite from water. ACS Appl. Mater. Int. 7, 26291–26300.

Gupta, K., Bhattacharya, S., Nandi, D., Dhar, A., Maity, A., Mukhopadhyay, A., Chattopadhyay, D.J., Ray, N.R., Sen, P., Ghosh, U.C., 2012. Arsenic(III) sorption on nanostructured cerium incorporated manganese oxide (NCMO): A physical insight into the mechanistic pathway. J. Colloid Interf. Sci. 377, 269–276.

He, Z., Tian, S., Ning, P., 2012. Adsorption of arsenate and arsenite from aqueous solutions by cerium-loaded cation exchange resin. J. Rare Earths 30, 563–572.

Ijagbemi, C.O., Baek, M.-H., Kim, D.-S., 2010. Adsorptive performance of un-calcined sodium exchanged and acid modified montmorillonite for Ni^{2+} removal: Equilibrium, kinetics, thermodynamics and regeneration studies. J. Hazard. Mater. 174, 746–755.

Jang, M., Min, S.H., Kim, T.H., Park, J.K., 2006. Removal of arsenite and arsenate using hydrous ferric oxide incorporated into naturally occurring porous diatomite. Environ. Sci. Technol. 40, 1636–1643.

Jang, M., Min, S.H., Park, J.K., Tlachac, E.J., 2007. Hydrous ferric oxide incorporated diatomite for remediation of arsenic contaminated groundwater. Environ. Sci. Technol. 41, 3322–3328.

Johansson, U., Holmgren, A., Forsling, W., Frost, R.L., 1999. Adsorption of silane coupling agents onto kaolinite surfaces. Clay Miner. 34, 239–246.

Kim, J.H., Bhattacharjya, D., Yu, J.-S., 2014. Synthesis of hollow TiO_2@N-doped carbon with enhanced electrochemical capacitance by an in situ hydrothermal process using hexamethylenetetramine. J. Mater. Chem. A 2, 11472–11479.

Kunzru, S., Chaudhuri, M., 2005. Manganese amended activated alumina for adsorption/oxidation of arsenic. J. Environ. Eng.-ASCE 131, 1350–1353.

Li, X.Z., Yao, C., Lu, X.W., Hu, Z.L., Yin, Y., Ni, C.Y., 2015. Halloysite-CeO_2-AgBr nanocomposite for solar light photodegradation of methyl orange. Appl. Clay Sci. 104, 74–80.

Liu, X., Zhang, G., Lin, L., Khan, Z.H., Qiu, W., Song, Z., 2018. Synthesis and characterization of novel Fe-Mn-Ce ternary oxide-biochar composites as highly efficient adsorbents for As(III) removal from aqueous solutions. Materials 11.

Liu, X., Gao, M., Qiu, W., Khan, Z.H., Liu, N., Lin, L., Song, Z., 2019. Fe-Mn-Ce oxide-modified biochar composites as efficient adsorbents for removing As(III) from water: Adsorption performance and mechanisms. Environ. Sci. Pollut. R. 26, 17373–17382.

Maity, S., Chakravarty, S., Bhattacharjee, S., Roy, B.C., 2005. A study on arsenic adsorption on polymetallic sea nodule in aqueous medium. Water Res. 39, 2579–2590.

Ngulube, T., Gumbo, J.R., Masindi, V., Maity, A., 2019. Preparation and characterisation of high performing magnesite-halloysite nanocomposite and its application in the removal of methylene blue dye. J. Mol. Struct. 1184, 389–399.

Ouyang, J., Zhao, Z., Zhang, Y., Yang, H., 2017. Textual properties and catalytic performances of halloysite hybrid CeO_2-ZrO_2 nanoparticles. J. Colloid Interf. Sci. 505, 430–436.

Peng, X.J., Luan, Z.K., Ding, J., Di, Z.H., Li, Y.H., Tian, B.H., 2005. Ceria nanoparticles supported on carbon nanotubes for the removal of arsenate from water. Mater. Lett. 59, 399–403.

Roehder, L.A., Brandt, T., Sigg, L., Behra, R., 2014. Influence of agglomeration of cerium oxide nanoparticles and speciation of cerium(III) on short term effects to the green algae *Chlamydomonas reinhardtii*. Aquat. Toxicol. 152, 121–130.

Rogers, N.J., Franklin, N.M., Apte, S.C., Batley, G.E., Angel, B.M., Lead, J.R., Baalousha, M., 2010. Physico-chemical behaviour and algal toxicity of nanoparticulate CeO_2 in freshwater. Environ. Chem. 7, 50–60.

Shan, C., Dong, H., Huang, P., Hua, M., Liu, Y., Gao, G., Zhang, W., Lv, L., Pan, B., 2019. Dual-functional millisphere of anion-exchanger-supported nanoceria for synergistic As(III) removal with stoichiometric H_2O_2: Catalytic oxidation and sorption. Chem. Eng. J. 360, 982–989.

Sharma, V.K., Sohn, M., 2009. Aquatic arsenic: Toxicity, speciation, transformations, and remediation. Environ. Int. 35, 743–759.

Sharma, R., Singh, N., Gupta, A., Tiwari, S., Tiwari, S.K., Dhakate, S.R., 2014. Electrospun chitosan-polyvinyl alcohol composite nanofibers loaded with cerium for efficient removal of arsenic from contaminated water. J. Mater. Chem. A 2, 16669–16677.

Shehzad, K., Ahmad, M., Xie, C., Zhan, D., Wang, W., Li, Z., Xu, W., Liu, J., 2019. Mesoporous zirconia nanostructures (MZN) for adsorption of As(III) and As(V) from aqueous solutions. J. Hazard. Mater. 373, 75–84.

Song, X., Zhou, L., Zhang, Y., Chen, P., Yang, Z., 2019. A novel cactus-like Fe3O4/Halloysite nanocomposite for arsenite and arsenate removal from water. J. Clean. Prod. 224, 573–582.

Tan, D., Yuan, P., Annabi-Bergaya, F., Yu, H., Liu, D., Liu, H., He, H., 2013. Natural halloysite nanotubes as mesoporous carriers for the loading of ibuprofen. Micropor. Mesopor. Mater. 179, 89–98.

Tan, D., Yuan, P., Annabi-Bergaya, F., Liu, D., Wang, L., Liu, H., He, H., 2014. Loading and in vitro release of ibuprofen in tubular halloysite. Appl. Clay Sci. 96, 50–55.

Thommes, M., Kaneko, K., Neimark, A.V., Olivier, J.P., Rodriguez-Reinoso, F., Rouquerol, J., Sing, K.S.W., 2015. Physisorption of gases, with special reference to the evaluation of surface area and pore size distribution (IUPAC Technical Report). Pure Appl. Chem. 87, 1051–1069.

Torres-Luna, J.A., Giraldo-Gomez, G.I., Sanabria-Gonzalez, N.R., Carriazo, J.G., 2019. Catalytic degradation of real-textile azo-dyes in aqueous solutions by using Cu-Co/halloysite. Bull. Mater. Sci. 42.

Wang, S., Mulligan, C.N., 2006. Occurrence of arsenic contamination in Canada: Sources, behavior and distribution. Sci. Total Environ. 366, 701–721.

Wang, M., Yu, X.L., Yang, C.L., Yang, X.Q., Lin, M.Y., Guan, L.T., Ge, M.F., 2017. Removal of fluoride from aqueous solution by Mg-Al-Zr triple-metal composite. Chem. Eng. J. 322, 246–253.

Wei, J., Zhu, R., Zhu, J., Ge, F., Yuan, P., He, H., Ming, C., 2009. Simultaneous sorption of crystal violet and 2-naphthol to bentonite with different CECs. J. Hazard. Mater. 166, 195–199.

White, R.D., Bavykin, D.V., Walsh, F.C., 2012. The stability of halloysite nanotubes in acidic and alkaline aqueous suspensions. Nanotechnology 23.

Xiong, W., Peng, J., 2008. Development and characterization of ferrihydrite-modified diatomite as a phosphorus adsorbent. Water Res. 42, 4869–4877.

Xu, W., Wang, J., Wang, L., Sheng, G., Liu, J., Yu, H., Huang, X.-J., 2013. Enhanced

arsenic removal from water by hierarchically porous CeO_2-ZrO_2 nanospheres: Role of surface- and structure-dependent properties. J. Hazard. Mater. 260, 498–507.
Ye, Z.F., Li, J.Z., Zhou, M.J., Wang, H.Q., Ma, Y., Huo, P.W., Yu, L.B., Yan, Y.S., 2016. Well-dispersed nebula-like ZnO/CeO_2@HNTs heterostructure for efficient photocatalytic degradation of tetracycline. Chem. Eng. J. 304, 917–933.
Yu, Y., Zhang, C., Yang, L., Chen, J.P., 2017. Cerium oxide modified activated carbon as an efficient and effective adsorbent for rapid uptake of arsenate and arsenite: Material development and study of performance and mechanisms. Chem. Eng. J. 315, 630–638.
Yuan, P., Southon, P.D., Liu, Z., Kepert, C.J., 2012a. Organosilane functionalization of halloysite nanotubes for enhanced loading and controlled release. Nanotechnology 23.
Yuan, P., Tan, D., Annabi-Bergaya, F., Yan, W., Fan, M., Liu, D., He, H., 2012b. Changes in structure, morphology, porosity, and surface activity of mesoporous halloysite nanotubes under heating. Clay Clay Miner. 60, 561–573.
Zeng, S., Reyes, C., Liu, J., Rodgers, P.A., Wentworth, S.H., Sun, L., 2014. Facile hydroxylation of halloysite nanotubes for epoxy nanocomposite applications. Polymer 55, 6519–6528.
Zhang, Y., Yang, M., Huang, X., 2003. Arsenic(V) removal with a Ce(IV)-doped iron oxide adsorbent. Chemosphere 51, 945–952.
Zhang, S., Li, X.-y., Chen, J.P., 2010. An XPS study for mechanisms of arsenate adsorption onto a magnetite-doped activated carbon fiber. J. Colloid Interf. Sci. 343, 232–238.
Zhang, L., Zhu, T., Liu, X., Zhang, W., 2016. Simultaneous oxidation and adsorption of As (III) from water by cerium modified chitosan ultrafine nanobiosorbent. J. Hazard. Mater. 308, 1–10.
Zhang, G., Xu, X., Ji, Q., Liu, R., Liu, H., Qiu, J., Li, J., 2017a. Porous nanobimetallic Fe-Mn cubes with high valent Mn and highly efficient removal of arsenic(III). ACS Appl. Mater. Inter. 9, 14868–14877.
Zhang, Q., Yang, Q., Phanlavong, P., Li, Y., Wang, Z., Jiao, T., Peng, Q., 2017b. Highly efficient lead(II) sequestration using size-controllable polydopamine microspheres with superior application capability and rapid capture. ACS Sustain. Chem. Eng. 5, 4161–4170.
Zhu, T., Zhu, T., Gao, J., Zhang, L., Zhang, W., 2017. Enhanced adsorption of fluoride by cerium immobilized cross-linked chitosan composite. J. Fluor. Chem. 194, 80–88.